Prediction of structure and phase transformations

Michael Widom

Abstract This chapter introduces calculational methods that can be used for ab-initio structure prediction in multicomponent alloy systems, with an emphasis on concepts relevant to high entropy alloys. Specifically we will address density functional-based calculation of T=0K total energies. Extension to finite temperature will utilize cluster expansions for the energies to obtain the chemical substitution entropy that characterizes the high entropy alloy family. Additional contributions such as vibrational and electronic entropies will be included as needed. We describe molecular dynamics and Monte Carlo simulation methods, and the types of information that can be obtained from them. Example applications include three high entropy alloy families, Cr-Mo-Nb-V, Nb-Ti-V-Zr, Mo-Nb-Ta-W, and their binary and ternary subsystems.

1 Introduction

High entropy alloys form when multiple chemical species intermix freely on a simple underlying crystal lattice, forming a thermodynamically stable single phase. However, most mixtures of chemical species will not form a high entropy alloy. Instead the mixtures separate into multiple distinct phases, and some of these phases might be complex crystal structures. Thermodynamic states of mixtures as functions of chemical composition and temperature are recorded in phase diagrams. While the stable crystal structures of almost all pure elements are known, as are the phase diagrams and crystal structures of most binary intermetallics, many ternary phase diagrams have not been determined, and almost no quaternary or higher phase diagrams are known. The discovery of high entropy alloys provides an opportunity to make progress on this scientific frontier.

Michael Widom
Department of Physics, Carnegie Mellon University, e-mail: widom@cmu.edu

This chapter outlines how basic physical principles can be used to predict the formation and stability of high entropy alloys. Conceptually the approach is straightforward. Every thermodynamic phase α has a Gibbs free energy G_α that depends on composition and temperature. We must calculate the free energies of different phases or combinations of phases and find the minimum. In practice we utilize quantum mechanics to calculate the total energy of specific crystal structures of interest, yielding the zero temperature limit of free energy. We then extend the free energy to finite temperature by using methods of statistical mechanics to include a variety of sources of entropy. Examples will be given drawn from mixtures of refractory elements. We will discuss certain binary compounds in detail, then move on to ternaries and finally quaternaries. The concepts and procedures described here generalize directly to non-refractory metals and to quinary and higher order alloy systems, although these lie outside the scope of this chapter.

Our approach differs from an alternative and highly successful method known as CALPHAD (see Chapter 12) for calculation of phase diagrams. CALPHAD utilizes databases of thermodynamic information based on experimental measurements (when available) supplemented by numerical interpolation schemes to fill in unknown territory. Ultimately CALPHAD should be merged with first principles total energy calculations to exploit the relative advantages of each. First principles excels at prediction of low temperature stability, obtaining enthalpies that while not exact are simply unavailable from experiment. CALPHAD excels at modeling of transition temperatures and phase diagram topology, as these are often determined experimentally with high reliability.

To illustrate these methods, we discuss in detail three overlapping examples of four-component alloy systems, comprised of refractory metals. We examine Mo-Nb-Ta-W, which is known to readily form a stable high entropy alloy [34]; Nb-Ti-V-Zr, which exhibits fine-grained second phase precipitation [33]; and Cr-Mo-Nb-V, which has not been considered experimentally to-date, but we predict should be stable at high temperature and decompose at low temperature. Understanding the quaternary alloy system requires, in addition, understanding all four ternary and all six binary subsystems. Indeed, our calculations confirm or shed new light on several experimentally known phase diagrams in addition to making some new predictions.

2 Total energy calculation, T=0K

Our goal in this section is to predict the T=0K limit of alloy phase diagrams by calculating the total energy of potential ground state structures and finding the minimum. Two major and distinct challenges arise immediately: 1) How to calculate the energy of a given crystal structure; 2) How to choose candidate structures whose energies should be determined. The first problem has a conceptually simple, though technically challenging answer. We will apply known laws of quantum mechanics that directly provide the desired quantity. The calculation will be made tractable through the use of well established approximations of density functional theory [26].

The second problem has no obvious solution. Although at a given composition there should be a unique minimum energy structure, we know of no method to predict what it will be. Since there are infinitely many conceivable structures, we cannot calculate all possibilities. Rather we will make a finite number of plausible guesses, based on a combination of physical intuition, chemical analogy and computer assisted search. This latter approach will exploit the fact that high entropy alloy families tend to form simple crystal lattices so that a cluster expansion of the total energy can accelerate our search for the ground state.

2.1 Density Functional Theory

Quantum mechanics tells us that the ground state energy of a system of interacting particles is the lowest eigenvalue of the system Hamiltonian. The Hamiltonian is an operator that expresses the total energy by adding together the kinetic and potential energies. For bulk matter we may separate atoms into positively charged nuclei, which are sufficiently massive that they may be treated as fixed point charges, and negatively charged electrons, whose mass is sufficiently low that they must be described through a position-dependent many-body wave function that is the eigenvector of the Hamiltonian. Electrons interact with each other and with the nuclei through the Coulomb potential. The eigenvalue equation to be solved is the Schroedinger equation of the system,

$$H\Psi^{(N)}(\mathbf{r}_1, \dots, \mathbf{r}_N) = E\Psi^{(N)}(\mathbf{r}_1, \dots, \mathbf{r}_N), \tag{1}$$

with $\Psi^{(N)}$ the many-body wave function.

The resulting interacting many-body problem, though well-posed, is computationally intractable owing to the high dimensionality of the Hilbert space in which the the many-electron wave function must be expressed. Hohenberg and Kohn [15] argued the many-body calculation could be replaced with the simpler problem of finding the electron density $\rho(r)$ that minimizes a total energy functional $E[\rho(r)]$. Kohn and Sham [21] re-expressed this minimization problem as a coupled set of single electron Schroedinger equations that can be solved individually (but self-consistently),

$$\left(\frac{-\hbar^2}{2m}\nabla_{\mathbf{r}}^2 + V_e(\mathbf{r}) + \int d\mathbf{r}' \frac{\rho(\mathbf{r}')}{|\mathbf{r}-\mathbf{r}'|} + V_{xc}[\rho(\mathbf{r})] \right) \psi_i(\mathbf{r}) = \varepsilon_i \psi_i(\mathbf{r}). \tag{2}$$

The terms on the left-hand side represent, respectively, the single electron kinetic energy, the "external potential" (electron-ion coupling), electron-electron interactions, and the "exchange-correlation potential". The equations for the single particle wavefunctions ψ_i are coupled through the electron density

$$\rho(\mathbf{r}) = \sum_{i=1}^{N} |\psi_i(\mathbf{r})|^2. \tag{3}$$

Although the replacement can be exact in principle, in practice the exact form of Eq. (2) is unknown, as it collects difficult to calculate effects of electron exchange and correlation into the unknown exchange-correlation potential $V_{xc}[\rho(r)]$ that is a functional of the electron density. The exchange correlation functional can be approximated to accuracy sufficient for our present purposes using the familiar local density approximation [3] (LDA) that replaces the exchange correlation functional with the value of the exchange correlation potential of a uniform electron gas whose density matches the local value of $\rho(r)$ or using the generalized gradient approximation [30] (GGA) that supplements the local density approximation with corrections dependent on the gradient of the density at the same point.

For the examples given in this chapter we solve the equations of density functional theory using a program known as VASP [22, 23]. This program exploits translational symmetry of crystal structures to express the single electron wave functions in a plane wave basis (i.e. a Fourier series). To ensure convergence of total energies we utilize dense k-point grids and truncate the basis at plane wave energy of 400 eV, significantly higher than the VASP defaults. We select the PBE generalized gradient approximation [30] also make an approximation that treats atomic core electrons approximately based on a variant of pseudopotential known as the Projector Augmented Wave method [2, 24].

No simpler approach is feasible for total energy calculation of high entropy alloys. Popular approaches such as pair potentials, embedded atom potentials, and similar empirical forms can be useful for modeling pure elements and even some binary compounds. Unfortunately these approximations contain adjustable parameters whose number proliferates with each additional chemical species, making them impossible to fit accurately as the number of chemical species increases. In contrast, the complexity and accuracy of density functional theory is relatively independent of the number of species present. The greatest utility of empirical potentials would be the study of abstract model systems whose properties can be defined for theoretical and computational convenience rather than realism.

2.2 Ground State Prediction

The lowest energy structure is known as the ground state and is the stable form of matter in the limit $T \to 0$K. Note that we adopt the absolute Kelvin scale of temperature throughout this chapter. Owing to the third law of thermodynamics (vanishing entropy) this structure is essentially unique for a given composition and pressure. Since we fix the pressure (generally at $P = 0$, which approximates atmospheric pressure) our energy is actually an "enthalpy"

$$H = \min_V [E(V) + PV], \tag{4}$$

and the corresponding free energy at finite temperature is the Gibbs free energy

$$G(T,P) = H - TS. \tag{5}$$

We need a notation for crystal structures. Among many possible schemes, we adopt the Pearson notation as especially convenient. The Pearson notation consists of: a lowercase letter a, m, o, t, h, c indicating, respectively, asymmetric, monoclinic, orthorhombic, tetragonal, hexagonal or cubic; an uppercase letter *PRFICBA* indicating primitive, rhombohedral or some type of centering; a number indicating the number of atomic sites per unit cell. For example, hP2 indicates HCP, while cI2 indicates BCC. Because many different compounds can form the same crystal structure, and *vice-versa*, we will append the Pearson symbol to the compound name to reduce ambiguity. Thus Cr.cI2 and Nb.cI2 are BCC chromium and niobium, while $Cr_2Nb.cF24$ and $Cr_2Nb.hP12$ are Laves phases (specific types of tetrahedrally close-packed Frank-Kasper phases), with hP12 being Strukturbericht C14 (prototype $MgZn_2$) and cF24 being Strukturbericht C15 (prototype Cu_2Mg).

The difficulty is finding the unique minimum enthalpy structure, because there are infinitely many conceivable arrangements among which we must find the minimum. Fortunately we often have experimental hints, as well as chemical and physical intuition and computer algorithms, that allow us to focus our search on a limited set of possibilities. By employing such constraints we risk the possibility that we exclude the true ground state and will always be confronted with an associated uncertainty in our predictions.

For most pure elements experimentalists voice little doubt about the stable form at low temperature and atmospheric pressure, and DFT calculations generally agree this form is the lowest in energy among competing possibilities [27] (elemental boron is a notable exception [40]). In many cases the elements undergo allotropic transitions to alternate structures as temperature rises. Notably, among the refractory metals in the Sc and Ti columns of the periodic table (groups IIIA and IVA), the ground state structure is a high density, close packed (FCC or HCP) structure. At higher temperatures the structure transforms to a lower density, loosely packed BCC structure. The mechanism for this transformation is the entropy thermal, as will be explained in detail in Sect. 3.2.
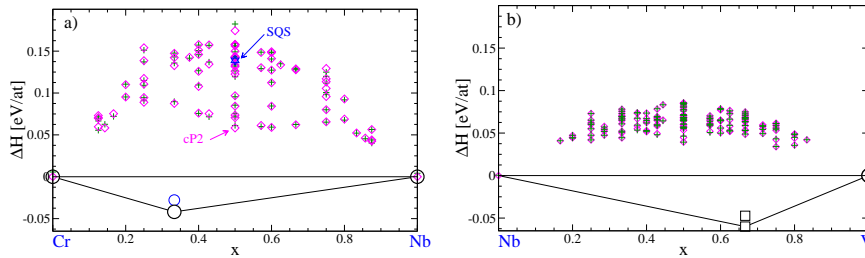

Fig. 1 Enthalpies of formation in the (a) Cr-Nb and (b) Nb-V binary alloy systems. Plotting symbols utilize thick circles for known low temperature stable phases, thin circles for known high temperature phases, squares for hypothetical structures, diamonds for representative structures of the BCC solid solution, and plus signs for cluster expansion fits.

Moving from pure elements to compounds introduces a composition variable x that is one-dimensional in the case of a binary compound but multidimensional in general. Many compounds exist as a pure phase at precise value or over a limited range of compositions x. The thermodynamic state at composition x between two pure phases of composition $x_\alpha < x < x_\beta$ consists of a mixture of the two phases α and β. Fig. 1a, which plots enthalpies of formation (enthalpy difference ΔH between the compound at composition x and the pure elements at compositions 0 and 1) of various structures containing elements Cr and Nb, illustrates the point. In this figure, $\Delta H < 0$ indicates structures whose enthalpy is lower than a mixture of pure crystalline Cr and Nb. Here we find two negative tnehalpy compounds, both at composition Cr_2Nb. At compositions with Nb content less than $x = 1/3$ the ground state corresponds to a mixture of two coexisting crystals, one of pure Cr.cI2, the other of pure Cr_2Nb.cF24. The enthalpy of formation of this mixture lies along the tie-line joining the enthalpy of formation of Cr_2Nb.cF24 to Cr.cI2. Similarly, at compositions $x > 1/3$ the ground state consists of Cr_2Nb.cF24 coexisting with Nb.cI2.

The vertices Cr.cI2, Cr_2Nb.cF24 and Nb.cI2, together with the line segments joining them constitute the convex hull of a scatter plot of formation enthalpy ΔH vs. composition x. This convex hull forms the sequence of predicted ground states as a function of composition. The structure Cr_2Nb.hP12 has a negative enthalpy of formation, indicating it is favorable to form from pure elements, but it lies above the convex hull by an amount $\Delta E = 0.01$ eV/atom, indicating it is thermodynamically unstable relative to the ground state. Indeed, the hP12 variant of Cr_2Nb is reported to be a high temperature stable phase.

Also visible in Fig. 1a are a variety of hypothetical crystal structures formed by decorating sites of a BCC lattice with Cr and Nb atoms in various specific repeating patterns. We shall refer to these structures as representative structures of the BCC solid solution. Keep in mind that the true solid solution is infinite in size and contains within it every possible finite representative structure. One specific such structure, known as a special quasirandom structure [43] (SQS, see Chapter 10) is chosen because its correlation functions closely match an idealized perfectly random distribution of Cr and Nb among the BCC lattice sites. The SQS can be considered as a realization of the disordered structure represented by the coherent potential approximation (CPA, see chapter 9). Another structure, which is the most ordered possible arrangement of two species on a BCC lattice, is cP2 (Strukturbericht B2, prototype CsCl) which places one species at cube vertices and the other species at cube centers. All of these decorated BCC lattices have positive enthalpy of formation indicating their formation is unfavorable at low temperature, although it is possible that some source of entropy could stabilize them at high temperature.

For convenience, we give here some representative energies of SQS and cP2 structures in three quaternary alloy families that we will focus on in this chapter, in addition to their binary and ternary subsystems.

Our ground state prediction remains tentative because it includes only finitely many trial structures. There is no guarantee that the experiment has found *all* the relevant structures, as it can be quite difficult to ensure the experimental samples remain in thermodynamic equilibrium, especially at low temperatures where atomic

Cr-Mo-Nb-V alloy system

Binary	SQS	cP2	cF24	T_m	Ternary	SQS	cF24	T_m	Quaternary	SQS	cF24	T_m
Cr-Mo	95	61	95	2093	Cr-Mo-Nb	65	46	2243	Cr-Mo-Nb-V	27	-22[†]	2180
Cr-Nb	139	62	-34	1893	Cr-Mo-V	-35	62	2105				
Cr-V	-50	-74	50	2040	Cr-Nb-V	81	-96	2022				
Mo-Nb	-71	-106	91	2742	Mo-Nb-V	-28	-40	2353				
Mo-V	-97	-118	17	2183								
Nb-V	63	55	-60*	2133								

Table 1 Representative formation enthalpies in the Cr-Mo-Nb-V quaternary and its subsystems. Units are meV/atom. Equiatomic SQS include a 16-atom structure for binaries [19], a 36-atom structure for ternaries [18] and a 16-atom structure for quaternary that has vanishing first and second neighbor correlations. Binary cP2 structure is CsCl-type (cP2). cF24 structures place smaller atoms on 16d sites, larger atoms on 8a (* is based on hP12, † has composition Cr_2MoNbV_2). Melting temperatures (units are K) are experimental minimum solidus temperatures for binaries, and averages are given for ternaries and quaternary.

Nb-Ti-V-Zr alloy system

Binary	SQS	cP2	cF24	T_m	Ternary	SQS	cF24	T_m	Quaternary	SQS	cF24	T_m
Nb-Ti	32	70	215	1943	Nb-Ti-V	63	84	1977	Nb-Ti-V-Zr	113	96	1884
Nb-V	63	55	-60*	2133	Nb-Ti-Zr	66	213	1929				
Nb-Zr	64	119	49	2018	Nb-V-Zr	133	38*	1892				
Ti-V	61	124	91	1855	Ti-V-Zr	143	100	1736				
Ti-Zr	53	113	201	1827								
V-Zr	164	233	43	1526								

Table 2 Representative formation enthalpies in the Nb-Ti-V-Zr quaternary and its subsystems. Other details as in Table 1.

Mo-Nb-Ta-W alloy system

Binary	SQS	cP2	T_m	Ternary	SQS	T_m	Quaternary	SQS	T_m
Mo-Nb	-71	-106	2742	Mo-Nb-Ta	-70	2793	Mo-Nb-Ta-W	-73	2885
Mo-Ta	-110	-186	2896	Mo-Nb-W	-58	2793			
Mo-W	-0.4	-10	2896	Mo-Ta-W	-97	3028			
Nb-Ta	-4	1	2742	Nb-Ta-W	-33	2926			
Nb-W	-34	-25	2742						
Ta-W	-67	-94	3293						

Table 3 Representative formation enthalpies in the Mo-Nb-Ta-W quaternary and its subsystems. Other details as in Table 1.

diffusion vanishes. A variety of alternative methods exist that aid in the exploration of potential ground states. Probably the most powerful, in the sense that the odds of success are high, is invoking chemical and geometrical analogy [27]. Another method for generating trial structures is known as genetic or evolutionary algorithms [11, 32]. This method generates random trials, then explores combinations of successful attempts to create new trials. While it has enjoyed some successes, its efficiency in general remains to be proven. Other methods include basin hopping [37] and minima hopping [12], which jump between nearby potential energy minima. A final method, the cluster expansion, proves quite effective for high entropy alloys, as we discuss below in section 2.3.

Among the columns of the periodic table starting with Ti, V and Cr, the reported structures include the hP2, cI2, cF24 and hP12 structures previously discussed. However, not every structure occurs in every combination of elements. An example of discovery by chemical analogy is illustrated in Fig. 1b, where we examine the same structures (cF24, hP12 and BCC-based structures) for Nb-V as we did previously for Cr-Nb. Here, we use square plotting symbols to indicate that cF24 and hP12 are hypothetical structures, proposed on the basis of chemical analogy. Although they have not been reported to occur experimentally, there is a clear energetic preference for NbV_2.hP12, well outside the expected errors of DFT formation enthalpies, which are typically a few meV/atom. In sections 3.1 and 3.2 below, we suggest an explanation for this discrepancy.

Noting that hP12 and cF24 are Laves (Frank-Kasper, F-K) phases characterized by tetrahedral close packing into specific clusters related to icosahedra, we invoke geometric analogy to investigate two other F-K structures, of Pearson types cP8 (A15) and hR13 (μ). We place the smaller Cr atoms at low coordination sites, while the larger Nb atoms occupy higher coordination sites. We find that the μ phase slightly outperforms the decorated BCC lattices, but in fact neither of these alternative F-K structures produce a new ground state for Cr-Nb, in agreement with experiment.

2.3 Cluster expansion

Because the high entropy alloys distribute multiple chemical species among sites of a common crystal lattice, we can use the underlying lattice structure to our advantage. The idea [4, 7, 42] is to represent the chemical species at each lattice site i with a variable σ_i (here for simplicity we take $\sigma_i = \pm 1$ for the case of two species), then expand the energy in a series of pair, three-body and higher interactions,

$$E(\sigma_1, \ldots, \sigma_n) = \sum_{\{i,j\}} J_{ij}\sigma_i\sigma_j + \sum_{\{i,j,k\}} J_{ijk}\sigma_i\sigma_j\sigma_k + \cdots. \tag{6}$$

The cluster interaction coefficients J can be fit to a database of DFT energies. Although the variables are assigned to lattice sites, it is important to note that the coefficients can be fit to *relaxed* energies, so that displacements off the ideal sites caused by size and chemical variation can be included. Given a cluster expansion it becomes quick and easy to estimate the energies of thousands of trial structures, then the best predictions can be checked with higher precision with a full DFT calculation. A convenient implementation of this method named the Alloy Theoretic Automated Toolkit [39, 38] (`ATAT`) has been placed in the public domain. This is the method that was used to generate the trial BCC decorations of Cr-Nb and Nb-V shown in Fig. 1.

The cluster expansion can be extended to multicomponent systems. Fig. 2 illustrates the case of the Cr-Nb-V ternary. Conveniently the databases of BCC energies

Fig. 2 Convex hull of the enthalpy of formation in the Cr-Nb-V alloy system. Predicted stable phases (convex hull vertices) are shown as black circles. Convex hull vertices are connected by tie-lines and by triangular tie-planes corresponding, respectively, to two- and three-phase coexistence regions. Structures above convex hull by $\Delta E < 100$ meV/atom are shown as blue diamonds, while higher energy structures are shown as red crosses.
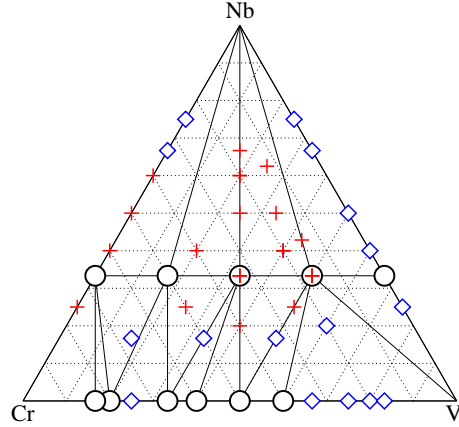
for the three binaries (Cr-Nb, Nb-V and Cr-V) can be re-used as the starting point
for the full ternary. In this figure, only the predicted lowest energy structure is shown
at each composition tested. The series of stable Cr-V binaries based on various pat-
terns of chemical order on the BCC lattice, demonstrate that formation enthalpies in
the Cr-V binary are negative [9, 10]. The stable $(Cr,V)_2Nb$ sequence has structure
cF24, except for V_2Nb which is hP12. Based on this data, we predict that at low
temperature any ternary combination of Cr-Nb-V will decompose into a mixture of
cF24 together with pure elemental or binary BCC-based structures. In the following
we utilize the cluster expansio to predict the behavior at high temperature.

3 Extension to finite temperature

In order to predict the phase behavior at high temperature we combine the quantum-
based energetics with principles of statistical mechanics and thermodynamics. Our
discussion will be easiest if we neglect thermal expansion. At constant volume the
relevant free energy is the Helmholtz free energy $F(V,T)$, which differs from the
Gibbs free energy by the Legendre transform

$$G(T,P) = \min_V [F(V,T) + PV], \tag{7}$$

similar to the relationship Eq. (4) of energy and enthalpy. The Helmholtz free energy
is given by the logarithm of the canonical partition function

$$F = -k_B T \ln Q, \tag{8}$$

where the partition function

$$Q = \frac{1}{N!} \left(\frac{2\pi m k_B}{h^2} \right)^{3N/2} Z \qquad (9)$$

factorizes into a contribution from the momenta times a configuration integral

$$Z = \int_V \prod_{i=1}^{N} d\mathbf{r}_i \; e^{-E(\mathbf{r}_1,\dots,\mathbf{r}_N)/k_B T}. \qquad (10)$$

The integrand in Eq. (10) is known as the Boltzmann factor, and is proportional to the probability of a given set of positions $(\mathbf{r}_1,\dots,\mathbf{r}_N)$. In the following we shall drop the momentum factors, as they are universal to all ordinary matter, and hence thermodynamically irrelevant.

Evaluation of the configuration integral Z is our main task. The position dependent energies $E(\mathbf{r}_1,\dots,\mathbf{r}_N)$ will be obtained from DFT. However, evaluation of the integral requires many evaluations of E, each of which is very time consuming. We will take advantage of the exponential dependence of the Boltzmann factor to make further approximations.

In crystalline solids atoms typically vibrate within small distances of their equilibrium positions. Indeed, the character of the energy landscape is such that it possesses a collection of local minima with approximately quadratic variation in the vicinity of each minimum. Each local minimum corresponds to a discrete arrangement of atoms that we shall refer to as a "configuration", while the small continuous displacements consist of mixtures of vibrational phonon modes. Temporarily restricting our attention to a single configuration Γ, we may evaluate the configuration integral $Z(\Gamma)$ by integrating over a neighborhood of Γ. In accordance with Eq. (8) we define the free energy of the configuration Γ as the logarithm $F(\Gamma) = -kT \ln Z(\Gamma)$, which we separate into the energy $E(\Gamma)$ of the discrete configuration Γ plus the vibrational free energy $F(\Gamma) = E(\Gamma) + F_v(\Gamma)$. Alternatively we may factorize the configuration integral into separate contributions from the energy of the configuration $E(\Gamma)$ and the vibrational free energy $F_v(\Gamma)$,

$$Z(\Gamma) = e^{-E(\Gamma)/k_B T} e^{-F_v(\Gamma)/k_B T}. \qquad (11)$$

Since the Boltzmann factor nearly vanishes far from the discrete configurations, the entire configurational integral can be approximated as a sum of integrals around each configuration. If we were to find that F_v depended only weakly on Γ, then in view of the factorization expressed in Eq. (11) we could pull a common factor out of the sum,

$$Z \approx \sum_{\Gamma} Z(\Gamma) \approx \left(\sum_{\Gamma} e^{-E(\Gamma)/k_B T} \right) e^{-F_v/k_B T} \equiv e^{-F_c/k_B T} e^{-F_v/k_B T} \qquad (12)$$

where we define $F_c = k_B T \ln Z_c$ with $Z_c = \sum_{\Gamma} e^{-E(\Gamma)/k_B T}$ as the partition function of the discrete configurational degrees of freedom. Finally, we note the separation

of the free energy into a discrete configurational part, and a contribution from the continuous vibrations, $F = -k_B T \ln Z = F_c + F_v$.

The preceding discussion assumed the integration in Eq. (10) was carried out at fixed volume V, and hence the resulting free energy was a Helmholtz free energy $F(N,V,T)$. Additionally integrating over the volume, including a factor $\exp(-PV/k_B T)$ in the integrand, takes us to a constant pressure ensemble, where the corresponding free energy is a Gibbs free energy $G(N,P,T)$. Equivalently we could perform the Legendre transform in Eq. (7). The decomposition into discrete configurational and continuous vibrational contributions follows as above, resulting in the decomposition $G = G_c + G_v$.

3.1 Example: configurational free energy

As an example of configurational free energy, consider the case of Nb-V. As seen in Fig. 1b, the representative structures of the BCC solid solution are all positive in energy, implying immiscibility, in seeming contradiction to the experimentally assessed phase diagram [35] which shows a continuous solid solution. However, the assessed phase diagram only goes down to $T = 2173\text{K}$. Indeed, experiments generally cannot achieve true equilibrium at temperatures far below their melting temperature. Meanwhile the ideal solid solution possesses $k\ln(2)$ of entropy suggesting entropic stabilization relative to phase separation at temperature $T = 0.063\text{eV}/k_B \ln(2) = 1055\text{K}$, where we take the SQS energy from Table 1 as a characteristic value. However, the actual energy and entropy of the solid solution cannot be estimated as simply as suggested in this paragraph. Short-range correlations in chemical occupation, related to the actual chemical interactions among constituents, will tend to reduce both the energy and entropy.
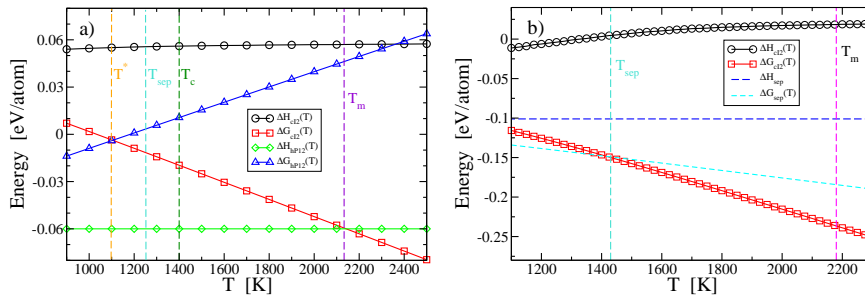

Fig. 3 (a) Thermodynamics of NbV$_2$. Enthalpy and configurational free energy of BCC (cI2) solid solutions are obtained from Monte Carlo simulations. Free energy ΔG_{hP12} of NbV$_2$ includes vibrational free energy from Eq. (14). T_m's are experimental melting temperatures. T_c is predicted critical temperature of Nb-V, while T_{sep} is phase separation temperature of NbV$_2$ and T^* is predicted temperature for stability of NbV$_2$.hP12. (b) Thermodynamics of CrMoNbV. Notation as in (a).

Monte Carlo simulation can properly deal with these correlations, by sampling all possible configurations weighted by their Boltzmann factors which favor energetically favorable structures. Fig. 3 illustrates results obtained using the `emc2` Monte Carlo program of the `ATAT` toolkit [38] in conjunction with energies defined by the cluster expansion obtained using the `maps` program [39]. We take as our initial condition a disordered arrangement of Nb and V on a $6 \times 6 \times 6$ BCC supercell, with global stoichiometry NbV_2. The ideal entropy of $S/k_B = (1/3)\ln(3) + (2/3)\ln(3/2) = \ln 1.89$ is slightly less than $\ln 2$ owing to the stoichiometry being non-equiatomic. Together with the initial energy of 0.058 eV/atom, this entropy determines the free energy at high temperatures. At fixed temperature T we attempt to swap positions between pairs of atoms of differing species, always accepting the swap if it lowers the total energy, and accepting with probability $\exp(-\Delta E/k_B T)$ if it raises the energy. The mean energy at temperature T provides the configurational contribution to the enthalpy, H_c, while thermodynamic integration provides the relative configurational free energy G_c between nearby temperatures. Note that the slope of $G_{cI2}(T)$ goes asymptotically to $\ln 1.89$ at high temperature. Note also that we may perform Monte Carlo at any desired temperature, including above the actual melting temperature, because we are simulating a lattice gas model with discrete configurations.

An alternative Monte Carlo method [38] attempts to swap the chemical identity of individual atoms, rather than interchanging positions of atom pairs. Since the total number of atoms is preserved, but not the global stoichiometry, this simulation occurs in the semi-grand ensemble. The `ATAT` program `phb` utilizes this method to identify the boundaries of coexisting phases. When applied to the case of Nb-V, this method confirms the existence of a low temperature miscibility gap, which closes in a critical point at temperature $T_c = 1400$K, far below the melting point. The phase boundary passes through stoichiometry NbV_2 at an even lower temperature, $T_{sep} = 1250$K. It is thus no surprise that experiments fail to identify phase separation in Nb-V, as this is predicted to occur far below the melting temperature which ranges from 2133K close to NbV_2 up to 2742K depending on composition, and hence equilibration will prove difficult. Similar conclusions were reached in an independent study [31].

According to the DFT calculated enthalpies, an additional competitor to the solid solution, other than phase separation, is formation of the predicted NbV_2.hP12 complex intermetallic, whose enthalpy of formation of -0.060 eV/atom lies on the convex hull implying stability in the limit of $T \to 0$K. Since the tetrahedral close packing exhibits sites of differing coordination number that favor specific chemical species, we assume this phase possesses no appreciable configurational entropy, and hence its configurational Gibbs free energy is simply given by its formation enthalpy, as indicated in Fig. 3. Notice that the solid solution free energy crosses the hP12 enthalpy at a temperature that happens to be close to the melting temperature. Accordingly, if vibrational free energy were to be neglected, hP12 would be expected to be the stable phase from T_m on down at composition NbV_2. The fact that NbV_2 has not been observed experimentally suggests that we must consider vibrational free energy, as we do below in section 3.2.

The reader may wonder why the solid solution beats $NbV_2.hP12$, but not $Cr_2Nb.cF24$, since the formation enthalpy of $NbV_2.hP12$ is even greater in magnitude than for $Cr_2Nb.cF24$. However, as can be seen in Fig. 1, the range of representative solid solution structure energies in Cr-Nb are nearly double those in Nb-V. The Monte Carlo simulated critical temperature of $T_c = 2950K$ lies far above the melting point $T_m = 1893K$. Although Cr exhibits 25% solubility in Nb, at higher Cr contrations the solid solution is unstable to the formation of $Cr_2Nb.cF24$. Thus we understand the high temperature Cr-Nb-V ternary phase diagram [36], which consists of BCC solid solutions along the Cr-V and Nb-V binary edges, while $Cr_2Nb.cF24$ is stable as a binary and extends stably far into the interior of the ternary composition space.

3.2 Example: vibrational free energy

The configurational integral Z in Eq. (10) restricted to the region of configuration space $nbd(\Gamma)$ surrounding the specific configuration Γ becomes

$$Z(c) = \int_{nbd(\Gamma)} \prod_{i=1}^{N} d\mathbf{r}_i e^{-E(\mathbf{r}_1,...,\mathbf{r}_N)/k_BT}. \tag{13}$$

and the free energy is $F(\Gamma) = -k_BT \ln Z(\Gamma)$. Provided that E varies quadratically in the vicinity of the local minimum Γ, the integrand becomes a Gaussian that can be integrated analytically. The resulting vibrational free energy is

$$F_v = k_BT \int g(\omega) \ln\left[2 \sinh\left(\hbar\omega/2k_BT\right)\right] d\omega \tag{14}$$

where $g(\omega)$ is the vibrational (phonon) density of states. In the limit of $T \to 0$ we find F_v consists entirely of the zero point energy of the harmonic phonon modes, while at elevated temperatures F_v grows negative. The form of this equation reveals that an excess of low frequency modes makes F_v grow negative rapidly, owing to a high vibrational entropy. We will restrict our discussion in this chapter to the harmonic approximation, whose validity diminishes at elevated temperature. The *quasi*harmonic approximation is a mild generalization that takes into account the volume-dependence of vibrational frequencies (Grüneisen parameters) and thus incorporates anharmonic effects leading to thermal expansion.

To compute the phonon spectrum we utilize the force constant method [25]. The force constants give the forces on one atom due to a displacement of another via the second derivative of total energy $\partial^2 U/\partial\mathbf{R}_i\partial\mathbf{R}_j$, which can be evaluated from density functional perturbation theory within VASP. We convert this to a dynamical matrix $\mathbf{D}(\mathbf{k})$ by weighting the rows and columns by inverse atomic masses, and then Fourier transforming at wavevector $\mathbf{k}$. Eigenvalues of the dynamical matrix are phonon frequencies $\omega(\mathbf{k})$, which can be converted into a density of states $g(\omega)$ by integrating over the Brillouin zone,

$$g(\omega) = \int_{BZ} \delta(\omega - \omega(\mathbf{k})) d^3\mathbf{k}. \tag{15}$$

In practice, we choose to sample the frequencies on a dense grid in **k**-space, then smear the distribution to approximate g. This procedure must be performed in a cell of sufficient size that all important interatomic force constants are represented.
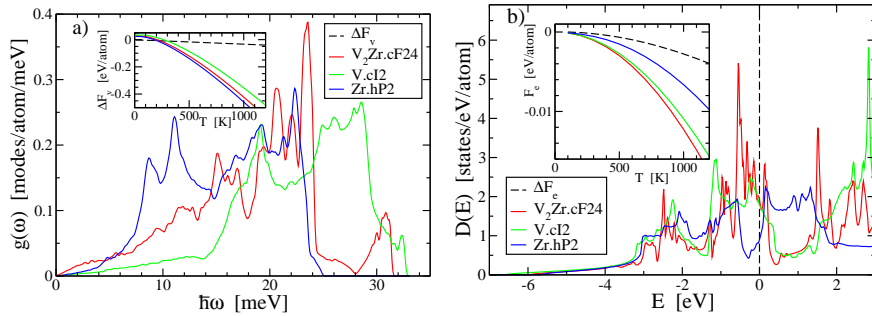

Fig. 4 Vibrational densities of states and free energies (left) and electronic densities of states and free energies (right) in the V-Zr alloy system

As a concrete example, consider the problem of stability of $V_2Zr.cF24$. The assessed phase diagram shows this phase as stable from low temperature up to 1592K. However, DFT calculations (Table 2) suggest a formation enthalpy of +43 meV/atom, indicating the state is unstable at low temperature. Probably this phase is actually stable only at high temperatures where it is formed, and simply remains metastable at low temperature. We need to find a source of entropy that can lower the free energy of the compound relative to the competing elements. Substitutional entropy is unlikely, as the two atomic species play distinct roles in this tetrahedrally close packed structure. The small V atoms center CN=12 icosahedra, while the larger Zr atoms center CN=16 polyhedra.

Fig. 4 compares the vibrational densities of states of the $V_2Zr.cF24$ compound with those of the pure elemental states V.cI2 and Zr.hP2. Owing to its large mass, Zr exhibits lower frequency modes, and hence more negative vibrational free energy, than the lower mass V, with V_2Zr falling in between. Although individual vibrational free energies are large, their *differences* are small, and comparable to the discrete configurational free energy. Combining the favorable vibrational free energy with the unfavorable formation enthalpy, $\Delta H + \Delta F_v$, we find that the V_2Zr compound is unstable to separation into pure elements below $T^* = 1290K$, but is stable above this temperature. One factor contributing to the vibrational entropy of $V_2Zr.cF24$ are the low frequency modes below 5 meV/atom. These reside predominantly on V atoms (counterintuitively, given the low V mass) and appear related to an unusually long V-Zr bond length in this structure.

Note that Zr undergoes an allotropic transition from its low temperature α (hP2) form to high temperature β (cI2) at $T = 1136K$, which is lower than the $T = 1290K$ at which we just predicted $V_2Zr.cF24$ becomes stable. Hence we should have com-

pared with the free energy of Zr.cI2 rather than hP2. Unfortunately Zr.cI2 is mechanically unstable, leading to phonon modes with imaginary frequencies ω. Eq. (14) cannot be utilized to calculate the vibrational free energy, requiring more sophisticated approaches [1, 5]. Alternatively, we can look up the NIST Janaf [29] table to find that the entropy jump at the α/β transition amounts to 3.7×10^{-5} eV/atom/K. Including this additional stability of β raises the predicted stability temperature of V_2Zr.cF24 to $T = 1380$K.

As a second example, recall the mysterious absence of NbV_2.hP12 from the experimental phase diagram despite its favorable enthalpy (Figs. 1b, 3a). Vibrational free energy provides the explanation. As a representative of the BCC solid solution we choose a specific structure of Pearson type tI6, and presume that its vibrational free energy is representative of the entire ensemble. Indeed, we find that the G_v of tI6 matches the composition-weighted G_v of pure Nb.cI2 and V.cI2 to within 2 meV/atom over the entire temperature range of interest (too low to be worth including in Fig. 3), despite the individual values reaching approximately -1.2 eV/atom at T_m, justifying our neglect of the structure-dependence within the solid solution. In striking contrast, the frequency spectrum of hP12 is shifted to high frequencies relative to BCC, owing to the tetrahedral close packing of the Laves phase contrasting with the loose packing of BCC. Consequently the vibrational free energy of hP12 greatly exceeds the pure elemental reference points, ΔF_v is *positive*, leading to the upwards slope of ΔG in Fig. 3, causing the free energy of hP12 to cross with the solid solution at $T^* = 1100$K. We predict that the BCC solid solution is thermodynamically stable from melting at $T_m = 2133$K down to the critical point for phase separation at $T_c = 1400$K. The hP12 Laves phase gains stability at a slightly lower temperature $T^* = 1100$K and remains stable down to $T = 0$K. The low temperature at which hP12 gains stability inhibits its formation experimentally.

Notice that the enthalpically favorable NbV_2.hP12 was *dstabilized* by F_v, while the enthalpically *un*favorable V_2Zr.cF24 was *stabilized*. Strong bonding, which lowers ΔH, increases vibrational frequencies ω, in turn raising F_v.

3.3 Electronic free energy

Excitations of the electron gas contribute entropy to an associated electronic free energy $F_e(T)$. Excitations are described by the Fermi-Dirac occupation function

$$f_T(E) = \frac{1}{1 + \exp[(E - \mu)/k_B T]} \tag{16}$$

representing the occupation probability f of states of energy E at temperature T given electron chemical potential μ. This function interpolates from full occupation ($f = 1$) for states below μ to complete vacancy ($f = 0$) for states above, with intermediate values restricted to energies within a few $k_B T$ of the chemical potential, which thus approaches the Fermi energy E_F at low T.

In combination with the electronic density of states, $D(E)$, obtained from first principles calculations, we can evaluate the electronic band energy and entropy

$$
\begin{aligned}
U(T) &= \int D(E)(E - E_F)(f_T(E) - f_0(E))\mathrm{d}E \\
S(T) &= -k \int D(E)[f_T(E)\ln f_T(E) + (1 - f_T(E))\ln(1 - f_T(E))]\mathrm{d}E,
\end{aligned}
\tag{17}
$$

and set $F_e(T) = U(T) - TS(T)$. Since low temperature excitations are restricted to the vicinity of E_F, the results are approximately proportional to the density of states at the Fermi level [20],

$$
U(T) \approx \frac{\pi^2}{6}D(E_F)k^2T^2, \quad S(T) \approx \frac{\pi^2}{3}D(E_F)k^2T, \quad F_e(T) \approx -\frac{\pi^2}{6}D(E_F)k^2T^2. \tag{18}
$$

The resulting quadratic variations are evident in Fig. 4, with coefficients proportional to $D(E_F)$. The electronic free energy difference yields a few meV/atom of additional stability to V_2Zr.cF24, bringing its temperature of instability down to $T^* = 1180K$. Notice that the individual electronic free energies are much smaller than the vibrational free energies, but the tendency towards cancelation is less pronounced, so the electronic contribution remains important.

4 Monte Carlo and molecular dynamics simulation

Molecular dynamics is well suited to reproduce the small amplitude oscillations of atoms in the vicinity of crystal lattice sites. At low temperatures the probability for an atom crossing the barrier from one lattice site to another is prohibitively low and will rarely occur on the time scale of a molecular dynamics run. In contrast, Monte Carlo swaps of atomic species on different sites occurs with a probability $P = \exp(-\Delta E/k_BT)$ related to the net energy difference $\Delta E = E_{swap} - E_{ini}$ of swapped and initial configurations, independently of the energy barrier separating the states. Since some of the pairwise interactions are quite low (see, e.g. Mo-W, Nb-Ta and Nb-W in Table 3, we expect that some Monte Carlo species swaps will be accepted even at low temperatures.

We implement this computationally by alternating molecular dynamics with Monte Carlo swaps [41], each performed from first principles using VASP. In the runs described below we perform 10 MD steps of 1 fs per time step, between each attempted species swap. As illustrated in Fig. 5 for Mo-Nb-Ta-W, swaps are frequently accepted with reasonably at moderate and high temperatures, indicating that the Monte Carlo achieves our goal of sampling the full configurational ensemble in the solid state. The same species swaps will almost never be observed via molecular dynamics. The utility of various hybrid MC/MD methods with empirical interaction potentials has been reviewed recently [28].

Fig. 5 Monte Carlo acceptance rates (ratio of accepted to attempted species swaps) for each species pair vs. temperature. Note correlation of high acceptance rate with low enthalpy values in Table 3.
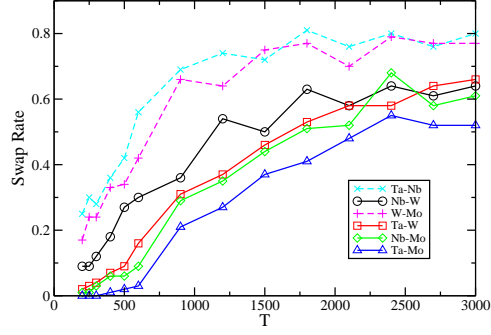
Swaps with the greatest size contrast (e.g. Ta-Mo and Nb-Mo) occur most infrequently, and are nearly absent at low temperatures, while the intermediate size swaps (Nb-W) occur occasionally and the most similar size swaps (e.g. Ta-Nb and W-Mo) occur with high probability even at the lowest temperatures. We conclude that at low temperature the system behaves nearly as a pseudobinary, consisting of the chromium group (group 5, here Ta and Nb) and the vanadium group (group 6, here W and Mo) as two effective species.

4.1 Pair correlation functions

Pair correlation functions describe the relative positional preferences of different atomic species. Their Fourier transforms yield the diffraction pattern, which is an important experimental probe of structure. Although crystalline solids are anisotropic, here we shall consider only the radial distribution function which measures the magnitudes of interatomic separations. The radial distribution function governs the angle averaged (i.e. powder) diffraction pattern. For chemical species α and β we define

$$g_{\alpha\beta}(r) = \frac{1}{N_\alpha N_\beta} \sum_{i=1}^{N_\alpha} \sum_{j=1}^{N_\beta} \langle \delta(|\mathbf{r}_{ij}| - r) \rangle. \tag{19}$$

In practice, a small amount of smearing is required to regularize the δ-functions.

Given a pair distribution function, the associated structure factor is

$$\tilde{h}_{\alpha\beta}(Q) = \int d\mathbf{r} e^{-i\mathbf{k}\cdot\mathbf{r}} (g_{\alpha\beta}(r) - 1), \tag{20}$$

and the total structure factor becomes

$$S(Q) = 1 + \sum_{\alpha\beta} c_\alpha f_\alpha c_\beta f_\beta \tilde{h}(Q), \tag{21}$$

where c_α is the concentration of species α. Here f_α is the form factor, which is approximately equal to the atomic number $f_\alpha = Z_\alpha$ for x-rays, or to the scattering length $f_\alpha = b_\alpha$ for neutrons.

4.2 Route to the entropy

Monitoring configuration statistics can yield estimates for the entropy. If the actual atomic positions can be mapped uniquely to nearby ideal lattice sites, then statistics on the occupation of each lattice site can be accumulated, along with statistics of various locally defined multisite clusters. Cluster variation methods [6, 8] have been developed as analytical approximations for the calculation of free energy given a model Hamiltonian. The general idea is to represent both the energy and the entropy, separately, as functions of the clusters. As the cluster size grows, the approximate free energy converges towards the exact value.

The simplest of these methods takes individual atomic sites as one-point clusters. Given N sites containing $N_\alpha = x_\alpha N$ atoms of species α, where α runs from 1 to m, and x_α is the concentration of species α. Counting the distinct occupations of sites (one-point clusters), yields the total number of configurations $g(\{N_\alpha\}) = \prod_\alpha N_\alpha!/N!$, Neglecting correlations among sites, the total entropy takes its maximal value

$$S(\{N_\alpha\})/k_B = \ln g = \ln N - \sum_\alpha \ln N_\alpha!. \tag{22}$$

Making the Stirling approximation, $\ln N! \approx N \ln N$ yields the entropy per site in the thermodynamic limit,

$$\sigma(\{x_\alpha\}) = \frac{-k}{N} S(\{N_\alpha\}) \approx -k \sum_\alpha x_\alpha \ln x_\alpha. \tag{23}$$

For an equiatomic composition of N species, so that $x_\alpha = 1/N$, this immediately yields the usual $S/k_B = \ln(N)$ entropy. Alternatively, we may take Eq. (23) as the local entropy density at any specific site. In this case, if individual sites exhibit a preference for specific elements (e.g. with the onset of chemical order) the values of x_α differ from $1/N$, and the entropy is reduced.

Moving to two-point clusters (nearest neighbor bonds) improves accuracy of the entropy as it corrects for the onset of short-range order. Guggenheim [13] calculated the number of configurations $g(\{N_\alpha\}, \{N_{\alpha\beta}\})$, where $N_{\alpha\beta}$ denotes the average number of β neighbors of atoms of chemical species α on a regular lattice of coordination number z. In the absence of correlations, we expect $N_{\alpha\beta} = N^*_{\alpha\beta} \equiv N_\alpha N_\beta/N$, and the actual number of configurations to equal $g(\{N_\alpha\})$. In the presence of correlations the reduced number of configurations is

$$g(\{N_\alpha\}, \{N_{\alpha\beta}\}) = g(\{N_\alpha\}) \prod_\alpha \frac{(zN_\alpha/2 - \sum_{\gamma \neq \alpha} N^*_{\alpha\gamma})!}{(zN_\alpha/2 - \sum_{\gamma \neq \alpha} N_{\alpha\gamma})!} \prod_{\alpha \neq \beta} \frac{N^*_{\alpha\beta}! 2^{N_{\alpha\beta}}}{N_{\alpha\beta}! 2^{N^*_{\alpha\beta}}}, \tag{24}$$

The multiplicative factors in Eq. (24) reduce the entropy due to deviations of the bond frequencies $N_{\alpha\beta}$ from their uncorrelated values $N^*_{\alpha\beta}$. As in the case of the single site cluster, this can be turned into a local entropy density

$$\sigma(\{N_\alpha\}, \{N_{\alpha\beta}\}) = k \ln g(\{N_\alpha\}, \{N_{\alpha\beta}\}). \tag{25}$$

Owing to the two point correlations, the global averages are nontrivial, in contrast to the single point case. They can be evaluated either by Monte Carlo simulation or estimated using the quasichemical approximation [13].

5 Structure and thermodynamic modeling of high entropy alloys

So far this chapter developed basic techniques that can in principle be applied to high entropy alloys, though the specific examples mainly concentrated on binary and ternary alloy systems. We now turn our attention to quaternary high entropy alloys, with a focus on BCC refractory metals, as example applications of the above methods.

The properties of the periodic table imply that metals whose positions are adjacent left/right or above/below tend to have similar size, valence and electronegativity, and hence substitute with relative ease for one another. Valency generally is constant within a column and differs by 1 between adjacent columns. Electronegativity correlates strongly with atomic volume, being low for large atoms and high for small atoms. The majority of elements in presently known high entropy alloys lie in proximity to each other on the periodic table, presumably exploiting the similarity in physical properties to increase their configurational entropy.

This observation motivates our choice to draw examples from 2×2 "squares" of the periodic table. That is, groups of four elements that lie on vertices of a unit square consisting of two adjacent elements of a row together with the two elements that lie directly below. In such a square the largest element will lie at the bottom left corner while the smallest is at the upper right corner. We shall call this the *positive* diagonal, while the top left to bottom right, which has smaller size contrast, will be called the *negative* diagonal.

5.1 Cr-Mo-Nb-V

Having previously discussed the binaries Cr-Nb and Nb-V in addition to the ternary Cr-Nb-V, we add a fourth element, Mo, to complete a 2×2 square consisting of the first two elements in the (V) column (namely V and Nb) and the first two elements of the adjacent (Cr) column (namely Cr and Mo). We extended our `ATAT` models of the binary and ternary subsystems to the full quaternary, running `maps` until the internal database extends to at least 8 atoms/unit cell and the true and predicted ground states

agree. Despite the SQS being at positive enthalpy, as listed in Table 1, `maps` was able to identify an equiatomic structure of negative enthalpy, -6 meV/atom. This lowest energy structure, which has Pearson type oI8, arranges the four chemical species on the BCC lattice in such a manner that each unit cell has 24 near neighbor pairs between columns (i.e. V-Cr, V-Mo, Nb-Cr or Nb-Mo) and only 8 near neighbor pairs within columns (i.e. V-V, V-Nb, Nb-Nb, Cr-Cr, Cr-Mo, or Mo-Mo). It thus exploits the preference for atoms of differing size and electronegativity to be nearest neighbors [41]. In general, the enthalpies of the cP2 structures lie below the SQS enthalpies (see Table 1), because cP2 and similar ordered structures can exploit preferred local chemical environments.

Despite the existence of negative enthalpy BCC representative structures, our DFT total energies predict that the ground state of equiatomic CrMoNbV consists of phase separation into four coexisting phases, raising questions concerning the possible existence of a high entropy alloy of this composition. No experimental report exists to-date.

Relative free energies of the BCC solid solution and the competing Laves phase are illustrated in Fig. 3b. The free energy of the solid solution was evaluated from Monte Carlo using `memc2` (the multicomponent version of `emc2` [38]), similarly to the case of NbV_2 discussed previously in section 3.1. A byproduct of the simulation is the ability to predict the entropy, in the present case by thermodynamic integration from a high temperature reference state. Assuming maximal entropy of $\ln(4)$ at $T = 3000K$, we obtain a nearly ideal $S/k_B = \ln(3.82)$ at T_m. The coexisting phases consist of three BCC-based structures, Cr_2V.tI6, Mo_4Nb_3.tI14 and Mo_4V_3.hR7, together with the Laves phase CrNbV.cF24, yielding the balanced equation

$$12\,CrMoNbV \;\rightarrow\; 3\,Cr_2V \;+\; 2\,Mo_4Nb_3 \;+\; 6\,CrNbV \;+\; Mo_4V_3 \qquad (26)$$

Taking the composition-weighted average of their enthalpies of formation predicts a ground state enthalpy of -101 meV/atom. We convert this into a finite temperature free energy by assuming ideal entropy of mixing at appropriate compositions for the three BCC-based structures, together with assumed Cr-V disorder in the Laves phase. As the entropies of all four competing phases are less than $\ln(2)$, the combination loses out to the high entropy alloy at high temperature, with phase separation expected only below $T_{sep} = 1430K$. There is considerable uncertainty in the precise separation temperature owing to several factors: we used the ideal entropy of mixing rather than the cluster expansion to evaluate the configurational entropies of the competing phases; we have neglected vibrational entropy throughout; some other combination of phases may exist whose enthalpy is less favorable but that has higher entropy.

MC/MD simulation results are shown in Fig. 6. Here we carry out the MC/MD simulation at $T = 1200K$, a temperature sufficiently high that chemical short-range order might be in equilibrium even in experiment. We then quench the system to $T = 300K$ and anneal under conventional molecular dynamics, where atomic diffusion is frozen out. Thus we freeze in short range order typical of the high annealing temperature, in an attempt to mimic the actual experiment. The figure illustrates the
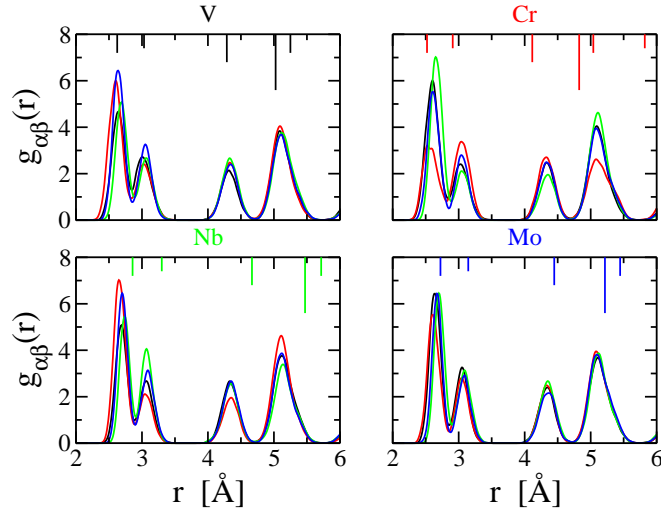
Fig. 6 Pair distribution functions of Cr-Mo-Nb-V at T=300K quenched from 1200K. Each panel shows the four partial pair correlation functions for the element named above. The partials are color coded, e.g. under V the black curve is V-V and the red curve is V-Cr. Bars at top indicate the corresponding correlations in the pure BCC element, e.g. V has 8 neighbors at $r = 2.6$ Å, 6 at 3.0, 12 at 4.3, 24 at 5.0 and 8 at 5.3.

four partial pair correlations for each of the four constituent elements, arranged on the page according to their positions on the periodic table. The BCC structure is clearly evident, with the well defined 8:6 split of nearest and next nearest neighbor peaks as well as well-defined further neighbor peaks. Also evident is the strong preference for intercolumn neighbors, with Cr and Mo forming the strongest near neighbor peaks of V and Nb, and *vice versa*.

Swap rates reported in Table 4 give insight into respective roles of different elements, with the swap rates being largest for elements that are most similar in size (the nearest off-diagonal) becoming progressively smaller as the size contrast grows more extreme, finally nearly vanishing for the pair Nb-Cr which constitutes the positive diagonal of the square as defined above. This table also gives the near-neighbor bond counts corresponding to the near-neighbor peaks in Fig. 6. We may use these bond counts in the formula Eq. (24) to evaluate the entropy at $T = 1200$K, which leads to $S/k_B = \ln(3.82)$, identical to the value obtained at T_m from `memc2`.

	Swap				Bonds			
$\alpha\backslash\beta$	Nb	Mo	V	Cr	Nb	Mo	V	Cr
Nb		0.48	0.24	0.05	1.73	2.05	1.71	2.51
Mo			0.49	0.23	2.00	1.90	2.14	1.96
V				0.43	1.86	2.21	1.79	2.14
Cr					2.41	1.84	2.36	1.39

Table 4 Monte Carlo swap rates and bond statistics for Cr-Mo-Nb-V quaternary at $T = 1200K$. Bond counts $N_{\alpha,\beta}$ count number of β-type neighbors of atom type α, where α labels rows and β labels columns. Elements are arranged in order of decreasing BCC lattice constant.

5.2 Nb-Ti-V-Zr

Our next square consists of the first two rows of the (Ti) column, namely Ti and Zr, together with the first two rows of the (V) column. This new compound provides an interesting example because Ti and Zr are HCP at low temperature but BCC at high temperature as a result of the lower enthalpy of HCP competing with the higher vibrational entropy of BCC (HCP is close-packed while BCC is loose packed). Meanwhile Nb and V are BCC at all temperatures. Can compounds formed from the (Ti) and (V) columns form HCP solid solutions, or must they form BCC? Fig. 7 provides a hint.

Application of the ATAT cluster expansion to predict low energy states of both BCC and HCP Nb-Zr alloys suggests complete phase separation into coexisting Nb.cI2 and Zr.hP2 in agreement with experiment at low temperature. However, in fig. 7 we see a large number of individual BCC configurations with energies of order 0.05 eV/atom. Clearly energy and configurational entropy favors a BCC solid solution over HCP at all but the most Zr-rich compositions. Applying emc2 within the BCC solid solution we identify a critical point for phase separation into Nb-rich and Zr-rich BCC phases at $T_c = 1250K$ and at a composition of 30% Zr. Experimentally the critical point lies at $T_c = 1258K$ and at a composition of 40% Zr.

Fig. 7 Enthalpy of formation in the Nb-Zr alloy system. Squares indicate representative structures of the BCC solid solution. SQS and cP2 are marked with special symbols. Hexagonal stars indicate HCP.
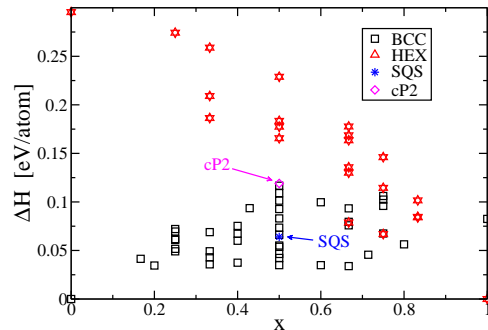
Fig. 8 shows the quaternary pair correlation functions obtained from MC/MD. Notice that in contrast to the case of CrMoNbV just discussed, here the 8:6 split of

nearest and next-nearest neighbor peaks is hardly evident, despite the longer range correlations beyond 4 Å remaining intact. This reflects the inherent mechanical instability of BCC-based structures containing Zr and Ti. A side effect is that the energies of the SQS structures in Table 2 generally lie *below* the energies of the cP2 structure, because the high symmetry of cP2 prevents lattice distortion. A similar severe distortion in the local BCC structure was seen experimentally in the HfNbZr ternary HEA [14]. Indeed, the BCC lattice is more visible in the V and Nb partials than in those containing Ti and Zr. Notice further that the strongest near neighbor correlation is between Zr and V, which lie along the positive diagonal of the square, while the partials of Ti and Nb are roughly similar, as is normal for the negative diagonal. This is further reflected in the Monte Carlo swap rates in Table 5, where Zr and V are almost unable to swap positions owing to their strong size contrast, while Ti and Nb swap easily. Applying the Guggenheim formulas to compute the $T = 1200K$ entropy yields $S/k_B = \ln(3.89)$, slightly greater than was observed in the case of CrMoNbV.
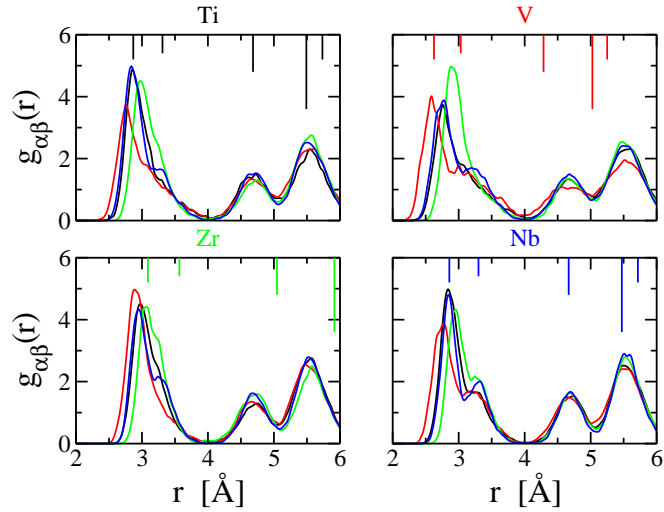

Fig. 8 Pair distribution functions of Nb-Ti-V-Zr at T=1200K quenched to $T = 300K$. Layout and conventions as in Fig. 6.

	Swap				Bonds			
$\alpha\backslash\beta$	Zr	Ti	Nb	V	Zr	Ti	Nb	V
Zr		0.32	0.29	0.07	1.60	2.03	1.96	2.41
Ti			0.59	0.39	1.96	2.10	2.10	1.83
Nb				0.34	1.98	2.27	1.98	1.89
V					2.57	1.59	1.96	1.88

Table 5 Monte Carlo swap rates and bond counts for Nb-Ti-V-Zr quaternary. Elements are arranged in order of decreasing BCC lattice constant.

5.3 Mo-Nb-Ta-W

As a final example, we choose a square from the bottom two rows of the (V) and (Cr) columns, namely Nb and Ta, and Mo and W. As previously shown [41], and reproduced in Table 3, the enthalpies of formation in this alloy system are significantly negative between columns and nearly zero within columns. Thus strong chemical order is anticipated, with the possibility of forming an ordered structure such as cP2 at low temperature, with the pair of elements from each column occupying its own sublattice. However, the very high melting temperature makes this phase difficult to observe experimentally. A mean field analysis of this transition [17] indicated a transition with a critical temperature of $T_c = 1600$K, although subsequent Monte Carlo simulations place it at 1280K [16] (mean field theory typically overestimates transition temperatures).

The cluster interaction model produced by `maps` predicts the equiatomic ground state structure is a coexistence of two BCC-based phases, $Mo_2NbTa_2W_2$.hR7 and pure elemental Nb.cI2, yielding the balanced equation

$$2\,MoNbTaW \;\rightarrow\; Mo_2NbTa_2W_2 \,+\, Nb. \tag{27}$$

Taking the composition-weighted average of the ground state enthalpy of formation yields enthalpy of -126 meV/atom. Monte Simulation using `memc2` yields the entropy at T_m as $S/k_B = \ln 3.93$.

MC/MD pair correlation functions shown in Fig. 9 reveal very strong BCC-like order including the 8:6 nearest to next-nearest neighbor split. As in the two previously examined cases, there is a pronounced preference for nearest neighbor pairs along the positive diagonal (Ta and Mo), while the partials for pairs along the negative diagonal (Nb and W) generally resemble each other. The effect is also seen in the swap rates reported in Table 6, with the pair along the positive diagonal swapping at far lower frequency than the pair along the negative diagonal. In keeping with the nearly zero interaction on pairs within columns, we notice very high swap rates for these pairs (Nb with Ta, and Mo with W).

Applying the Guggenheim formulas, we estimate the entropy at $T = 1200$K as $S/k_B = \ln(3.82)$, again similar to the value obtained for CrMoNbV. Full temperature dependence of the entropy is plotted in Fig. 5 and can be seen to decrease significantly only below 1200K. Given the existence of a ground state at nearly the equiatomic composition, we can say that MoNbTaW is an essentially perfect high
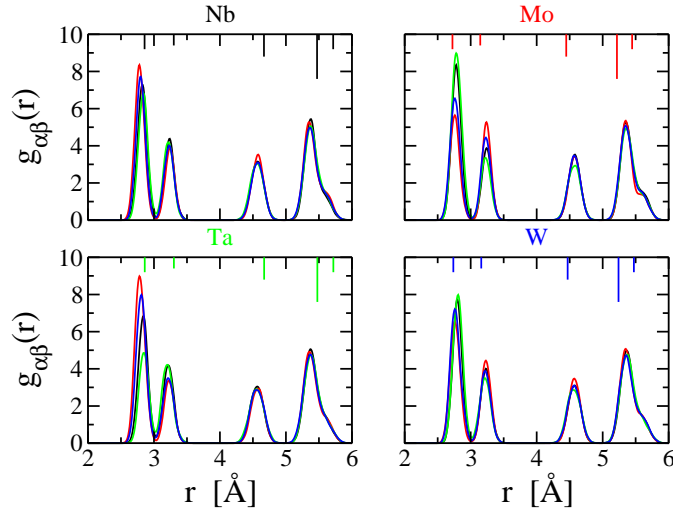
Fig. 9 Pair distribution functions of Mo-Nb-Ta-W at $T = 1200$K quenched to $T = 300$K. Layout and conventions as in Fig. 6.

entropy alloy that remains stable at all temperatures, with only minor shift in composition. At the same time, the entropy does vanish in this low temperature limit, with the growth of short-range chemical order, notably an increase in intercolumn bonds.

	Swap				Bonds			
$\alpha \backslash \beta$	Ta	Nb	W	Mo	Ta	Nb	W	Mo
Ta		0.74	0.37	0.27	1.39	1.90	2.20	2.51
Nb			0.54	0.35	1.84	1.95	2.11	2.10
W				0.64	2.18	1.93	1.99	1.90
Mo					2.59	2.22	1.70	1.49

Table 6 Monte Carlo swap rates and bond counts for Mo-Nb-Ta-W quaternary. Elements are arranged in order of decreasing BCC lattice constant.

Vibrational and electronic densities of states, and the resulting free energies are presented in Fig. 10. Notice that the relative vibrational free energy ΔF_v is positive, owing to the relatively high vibrational frequencies, and likewise the relative electronic free energy ΔF_e is positive because of the relatively low density of states at the Fermi level. Because these have been derived at fixed volume V, the free energies are Helmholtz free energies, hence thermodynamics yields the entropy by simple differentiation, $S = -\partial F/\partial T$, so we see that electronic and vibrational contributions actually *reduce* the entropy.
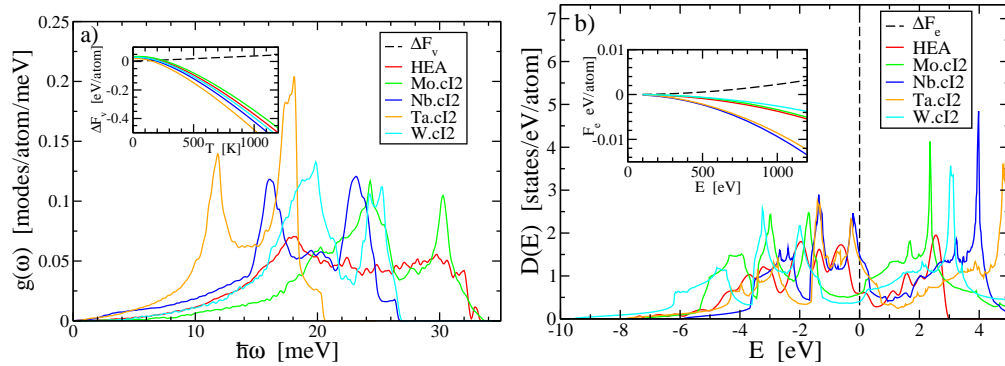
Fig. 10 Vibrational densities (a) of states and free energies (left) and electronic densities of states and free energies (b) in the MoNbTaW HEA.

6 Conclusion

This chapter provides a brief introduction to first principles approaches to free energy and phase stability calculation, with application to three high entropy alloy-forming quaternary compounds. We describe and apply a variety of methods including the cluster expansion of total energy as implemented in the ATAT toolkit in section 2.3, vibrational and electronic free energy calculation in sections 3.2 and 3.3, and a hybrid Monte Carlo/molecular dynamics method in section 4 that is specifically efficient for systems such as HEA's where chemical substitution proliferates. Later chapters cover some additional first principles methods in detail, the coherent potential approximation (CPA) in chapter 9 and special quasirandom structures (SQS) in chapter 10, as well as application of the MC/MD method to liquids in chapters 11 and 13. The thermodynamic data calculated using the present methods can be a guide to the refinement of CALPHAD-type thermodynamic databases such as employed in chapter 12, which eventually provide the rigorous basis for formation rules such as those described in chapter 2.

Although the intent was tutorial, this chapter reports several new results, illustrating the potential for new discovery in this emerging field of research. Two specific results challenge or shed new light on assessed binary phase diagrams. Namely, we propose that the continuous BCC solid solution in Nb-V is replaced by a previously unknown C14 Laves phase, NbV_2.hP12, below $T^* = 1100K$, and we explain the occurrence of the C15 Laves phase V_2Zr.cF24, despite its unfavorable enthalpy of formation, as a result of vibrational and electronic entropy above $T^* = 1180K$, while predicting it becomes thermodynamically unstable below this temperature. Through the use of cluster expansions of total energy, we predicted the existence of low temperature stable quaternaries in the Mo-Nb-Ta-W alloy system. These new structures are specific ordered arrangements of species close to sites of the underlying BCC lattice. In the case of Cr-Mo-Nb-V, we found that all BCC-based quaternary structures were destabilized at low temperature by competing binaries and ternaries, but

we predict this compound forms a high entropy alloy that is stable above the temperature $T_{sep} = 1430K$. Because Ti and Zr prefer HCP structures at low temperatures, there are likewise no BCC-based ground states in the quaternary Nb-Ti-V-Zr, so this HEA is also unstable at low temperature. Indeed, we show through MC/MD simulations that the Nb-Ti-V-Zr HEA exhibits strong deviations from ideal lattice sites, even while preserving the long range BCC structure.

To conclude this chapter we present all contributions to the entropy for the quaternary Mo-Nb-Ta-W. The discrete configurational entropy is evaluated from Eq. (25) while the vibrational and electronic free energies were obtained from the free energies illustrated in Fig. 10 by differentiation, $S = -\partial F(V,T)/\partial T$. The corresponding entropies are shown in Fig. 11. For this particular compound, the vibrational and electronic entropies turn out to be *negative* relative to a mixture of pure elements. Notice that the electronic contribution is relatively small, while the vibrational contribution is significant, but still less than the configurational part, validating the claim that high entropy alloys are dominated by their configurational entropy of mixing.
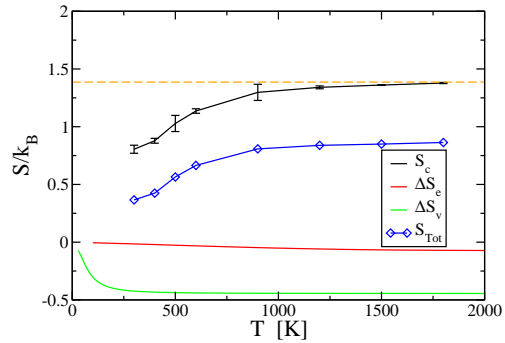

Fig. 11 Configurational, vibrational and electronic contributions to the total entropy S_{Tot}. Configurational entropy calculated according to the Guggenheim approximation Eqs. (24) and (25). Vibrational and electronic contributions come from Eqs. (14) and (18), respectively.

References

[1] Antolin N, Restrepo OD, Windl W (2012) Fast free-energy calculations for unstable high-temperature phases. Phys Rev B 86:054,119

[2] Blochl PE (1994) Projector augmented-wave method. Phys Rev B 50:17,953–79

[3] Ceperley DM, Alder BJ (1980) Ground state of the electron gas by a stochastic method. Phys Rev Lett 45:566–569

[4] Ducastelle F (1991) Order and phase stability in alloys. Elsevier

[5] Errea I, Calandra M, Mauri F (2014) Anharmonic free energies and phonon dispersions from the stochastic self-consistent harmonic approximation: Application to platinum and palladium hydrides. Phys Rev B 89:064,302

[6] de Fontaine D (1979) Configurational thermodynamics of solid solutions. In: Ehrenreich H, DTurnbull (eds) Solid State Physics, vol 34, Academic Press, pp 73–274

[7] de Fontaine D (1994) Cluster approach to order-disorder transformation in alloys. Solid State Physics 47:33

[8] de Fontaine D (1994) Cluster approach to order-disorder transformations in alloys. In: Ehrenreich H, DTurnbull (eds) Solid State Physics, vol 47, Academic Press, pp 33–176

[9] Gao M, Dogan O, King P, Rollett A, Widom M (2008) First principles design of ductile refractory alloys. J of Metals 60:61–5

[10] Gao M, Suzuki Y, Schweiger H, Dogan O, Hawk J, Widom M (2013) Phase stability and elastic properties of cr-v alloys. J Phys: Condens Matter 25:075,402

[11] Glass CW, Oganov AR, , Hansen N (2006) Uspex - evolutionary crystal structure prediction. Comp Phys Comm 175:713–20

[12] Goedecker S (2004) Minima hopping: An efficient search method for the global minimum of the potential energy surface of complex molecular systems. J Chem Phys 120:9911–7

[13] Guggenheim EA (1944) Statistical thermodynamics of mixtures with non-zero energies of mixing. Proc Roy Soc London A 183:213–27

[14] Guo W, Dmowski W, Noh JY, Rack P, Liaw PK, Egami T (2013) Local atomic structure of a high-entropy alloy: An x-ray and neutron scattering study. Met Mat Trans A

[15] Hohenberg P, Kohn W (1964) Inhomogeneous electron gas. Phys Rev 136(3B):864–871

[16] Huhn WP (2014) Thermodynamics from first principles: Prediction of phase diagrams and materials properties using density functional theory. PhD thesis, Carnegie Mellon University

[17] Huhn WP, Widom M (2013) Prediction of a2 to b2 phase transition in the high entropy alloy monbtaw. JOM 65:1772–9

[18] Jiang C (2009) First-principles study of ternary bcc alloys using special quasirandom structures. Acta Mater 57:4716–26

[19] Jiang C, Wolverton C, Sofo J, Chen LQ, Liu ZK (2004) First-principles study of binary bcc alloys using special quasirandom structures. Phys Rev B 69:214,202

[20] Kittel C (2005) Introduction to Solid State Physics. Wiley

[21] Kohn W, Sham LJ (1965) Self-consistent equations including exchange and correlation effects. Phys Rev 140:1133–8

[22] Kresse G, Furthmuller J (1996) Efficient iterative schemes for ab initio total-energy calculations using a plane- wave basis set. Phys Rev B 54:11,169–86

[23] Kresse G, Hafner J (1993) Ab initio molecular dynamics for liquid metals. Phys Rev B 47:RC558–61

[24] Kresse G, Joubert D (1999) From ultrasoft pseudopotentials to the projector augmented-wave method. Phys Rev B 59:1758–75

[25] Kresse G, Furthmuller J, Hafner J (1995) Ab initio force constant approach to phonon dispersion relations of diamond and graphite. Europhys Lett 32:729–34

[26] Martin R (2008) Electronic Structure: Basic theory and practical methods. Cambridge

[27] Mihalkovič M, Widom M (2004) Ab-initio cohesive energies of fe-based glass-forming alloys. Phys Rev B 70:144,107

[28] Neyts EC, Bogaerts A (2013) Combining molecular dynamics with monte carlo simulations: implementations and applications. Theor Chem Acc 132:1–12

[29] NIST (2013) Janaf thermochemical tables, http://kinetics.nist.gov/janaf

[30] Perdew JP, Burke K, Ernzerhof M (1996) Generalized gradient approximation made simple. Phys Rev Lett 77:3865–3868, DOI 10.1103/PhysRevLett.77.3865, URL http://link.aps.org/doi/10.1103/PhysRevLett.77.3865

[31] Ravi C, Panigrahi BK, Valsakumar MC, van de Walle A (2012) First-principles calculation of phase equilibrium of v-nb, v-ta, and nb-ta alloys. Phys Rev B 85:054,202

[32] Revard BC, Tipton WW, Hennig RG (2014) Structure and stability prediction of compounds with evolutionary algorithms. Topics in current chemistry 345:181–222

[33] Senkov O, Senkova S, Woodward C, Miracle D (2013) Low-density, refractory multi-principal element alloys of the crnbtivzr system: Microstructure and phase analysis. Acta Mater 61:1545–57

[34] Senkova O, Wilks G, Miracle D, Chuang C, Liaw P (2010) Refractory high-entropy alloys. Intermetallics 18:1758–65

[35] Smith JF, Carlson ON (1990) Nb-v (niobium-vanadium). In: Massalski TB (ed) Binary Alloy Phase Diagrams, II edition, ASM, pp 2779–82

[36] Takasugi T, Yoshida M, Hanada S (1995) Microstructure and high-temperature deformation of the c15 nbcr2-based laves intermetallics in nb-cr-v alloy system. J Mat Res 10:2463–70

[37] Wales DJ, Doye JPK (1997) Global optimization by basin-hopping and the lowest energy structures of lennard-jones clusters containing up to 110 atoms. J Phys Chem A 101:5111–6

[38] van de Walle A, Asta M (2002) Self-driven lattice-model monte carlo simulations of alloy thermodynamic properties and phase diagrams. Modelling Simul Mater Sci Eng 10:521

[39] van de Walle A, Ceder G (2002) Automating first-principles phase diagram calculations. J Phase Equil 23:348

[40] Widom M, Mihalkovic M (2008) Symmetry-broken crystal structure of elemental boron at low tempearture. Phys Rev B 77:064,113

[41] Widom M, Huhn W, Maiti S, Steurer W (2013) Hybrid monte carlo/molecular dynamics simulation of a refractory metal high entropy alloy. Mat Met Trans A 45:196–200

[42] Zunger A (1994) NATO ASI on Statics and Dynamics of Alloy Phase Transformation, eds. P. E. Turchi and A. Gonis, vol 319, Plenum, chap First principles statistical mechanics of semiconductor alloys and intermetallic compounds., p 361

[43] Zunger A, Wei SH, Ferreira LG, Bernard JE (1990) Special quasirandom structures. Phys Rev Lett 65:353–356